PNAS RESEARCH ARTICLE | BIOPHYSICS AND COMPUTATIONAL BIOLOGY CHEMISTRY

Structural basis for coupled ATP-driven electron transfer in the double-cubane cluster protein

Jae-Hun Jeoung[a], Sabine Nicklisch[a], and Holger Dobbek[a,1]

Edited by Douglas Rees, HHMI, California Institute of Technology, Pasadena, CA; received February 28, 2022; accepted June 22, 2022

Electron transfers coupled to the hydrolysis of ATP allow various metalloenzymes to catalyze reductions at very negative reduction potentials. The double-cubane cluster protein (DCCP) catalyzes the reduction of small molecules, such as acetylene and hydrazine, with electrons provided by its cognate ATP-hydrolyzing reductase (DCCP-R). How ATP-driven electron transfer occurs is not known. To resolve the structural basis for ATP-driven electron transfer, we solved the structures of the DCCP:DCCP-R complex in three different states. The structures show that the DCCP-R homodimer is covalently bridged by a [4Fe4S] cluster that is aligned with the twofold axis of the DCCP homodimer, positioning the [4Fe4S] cluster to enable electron transfer to both double-cubane clusters in the DCCP dimer. DCCP and DCCP-R form stable complexes independent of oxidation state or nucleotides present, and electron transfer requires the hydrolysis of ATP. Electron transfer appears to be additionally driven by modulating the angle between the helices binding the [4Fe4S] cluster. We observed hydrogen bond networks running from the ATP binding site via the [4Fe4S] cluster in DCCP-R to the double-cubane cluster in DCCP, allowing the propagation of conformational changes. Remarkable similarities between the DCCP:DCCP-R complex and the nonhomologous nitrogenases suggest a convergent evolution of catalytic strategies to achieve ATP-driven electron transfers between iron–sulfur clusters.

complex formation | ATP-dependent reduction | signal transduction | iron–sulfur cluster | double-cubane cluster

Significance

The reduction of molecules at negative reduction potentials is a necessity and a challenge in biology and chemistry. The electrons required for the reduction may be energized by coupling the reaction(s) to an exergonic process such as the fission of reactive bonds in compounds like ATP. Our study of different complexes between an ATP-hydrolyzing reductase and its associated negative reduction–potential electron acceptor reveal very similar spatial arrangements of functional elements within unrelated proteins, pointing to a convergent evolution of catalytic strategies. Their architectures allow conformational changes at the ATP-binding/hydrolysis site to be propagated within the complex.

In biological redox reactions, reductive activation of inert molecules at metal clusters often demands an energy input to drive thermodynamically uphill electron transfers (ETs), with ATP hydrolysis being one commonly used energy source. Three different metallo-ATPase classes evolved independently in nature to couple the exergonic ATP hydrolysis to ET (1): 1) the nitrogenase reductases (Fe protein) and homologs (2–4), 2) the reductive activators of corrinoid-containing enzymes (RACEs) (5–8), and 3) a class comprising ATP-dependent benzoyl-coenzyme A reductase (BCR) (9, 10), reductive activators of 2-hydroxyacyl-CoA dehydratases (HADs) (11, 12), and double-cubane cluster protein reductases (DCCP-Rs) (13). The common feature of all three classes is that they comprise two components: an ATPase acting as an electron donor and an electron acceptor catalyzing the principal substrate turnover.

Most widely known is the MoFe nitrogenase, which reduces dinitrogen to ammonia at the [Mo7Fe9SC-homocitrate] cluster. The reduction of one dinitrogen molecule is coupled to the hydrolysis of 16 ATP to transport eight electrons from the Fe protein to the MoFe nitrogenase (2, 14–16). In this complex interplay, the Fe protein, a member of the P-loop nucleoside triphosphate hydrolases (NTPase) family (17), controls complex association/dissociation, inter/intra ET, ATP binding/hydrolysis, and adenosine diphosphate and phosphate (ADP/Pi) release during the multielectron transfer, which together constitute the Fe protein cycle (2, 4, 18–21). A similar architecture as in the MoFe nitrogenase is found in the homologous VFe nitrogenase (22–24) and protochlorophyllide oxidoreductase (25).

A second class of electron-transferring metallo-ATPases are the RACE-type ATPases, which belong to the acetate and sugar kinases/heat shock protein 70/actin (ASKHA)-type ATPases (5–8). These ATPases reduce the inactive Co^{2+} state of corrinoid-containing enzymes, reverting it to the active Co^{+} state (5–8). Complex formation between the partners is controlled by the oxidation state and the presence of nucleotides (8, 26–28), where the binding of ATP can trigger electron transfer (29).

HADs and BCRs belong to the third class of electron-transferring metallo-ATPases (10, 30, 31). HADs and BCRs are Fe/S-containing enzymes, comprising a metallo-ATPase of the ASKHA superfamily and the catalytic enzyme that catalyzes a radical-dependent reaction (9, 10, 32, 33). While the catalytic reaction of BCRs is a reduction and requires stoichiometric ATP hydrolysis, the dehydration reaction of HADs only

Author affiliations: [a]Department of Biology, Humboldt-Universität zu Berlin, 10099 Berlin, Germany

Author contributions: J.-H.J. and H.D. designed research; J.-H.J. and S.N. performed research; J.-H.J. and H.D. analyzed data; and J.-H.J. and H.D. wrote the paper.

The authors declare no competing interest.

This article is a PNAS Direct Submission.

[1]To whom correspondence may be addressed. Email: holger.dobbek@biologie.hu-berlin.de.

This article contains supporting information online at http://www.pnas.org/lookup/suppl/doi:10.1073/pnas.2203576119/-/DCSupplemental.

Published July 29, 2022.

requires a catalytic electron with the metallo-ATPase acting as a reductive activator of the catalytic unit. In contrast to the stable complex in BCRs, the complex formation between ATPase and the catalytic unit in HADs is nucleotide-dependent (31, 33). For HADs, the crystal structures of the activators showed that in each subunit a helix pointing to the bridging [4Fe4S] cluster formed a defined helix–cluster–helix (HCH) angle that could change with nucleotide binding (33, 34). If the HCH angle was to widen to 180°, then it could catapult the electron out like the sinew of a bow. The ATPases were therefore also called "archerases" (11, 12).

Double-cubane cluster proteins (DCCPs) belong to the same enzyme class as HADs and BCRs. They also comprise two components: the catalytic DCCP and the associated ATP-dependent reductase DCCP-R (1, 13). While the physiological function of DCCPs is unknown, they can catalyze reactions with high activation energy, such as the reduction of acetylene, hydrazine, and azide at a fused double-cubane cluster (DC cluster) [4Fe4S]-μ_2S-[4Fe4S]. The DC cluster cannot be reduced by typical low-potential reducing agents, such as Na-dithionite (DT) or Ti(III) citrate (13).

How ATP hydrolysis and electron transfer are coupled in the HAD/BCR/DCCP class is still not understood. To identify the interplay between the nucleotide-binding site, the electron donor, and acceptor clusters, we determined the structure of the DCCP:DCCP-R complex in different states and showed how the spatial arrangement of the cofactors may couple the hydrolysis of ATP to the reduction of the DC cluster.

Results

Complex formation of DCCP-R with DCCP and with nucleotide. Because ATP-dependent reductases and their partners form complexes whose stability may depend on the redox state or the bound nucleotide, we investigated the complex formation between DCCP and DCCP-R under different conditions using analytical size–exclusion chromatography (SEC) and isothermal titration calorimetry (ITC). SEC showed that DCCP and DCCP-R exist as homodimers in solution and form stable complexes (DCCP:DCCP-R), regardless of the presence of nucleotides or the redox state of the proteins (*SI Appendix*, Fig. S1 and Table S1). The apparent molecular weight (94–101 kDa) indicates a 1:1 protein complex. When we increased the ionic strength in the SEC running buffer to 500 mM KCl, the DCCP:DCCP-R complex was destabilized as evident by the tailing of the elution profile (*SI Appendix*, Fig. S1 *C* and *D* and Table S1). This destabilization by increased salt concentrations suggests that the DCCP:DCCP-R complex is, at least partially, stabilized by electrostatic interactions, which are disrupted at higher salt concentrations.

The stability of the complex between DCCP and DCCP-R was further investigated by ITC, where we analyzed the effect of two different nucleotides, MgADP and MgADPNP (ATP-analog, 5′-adenylyl β, γ-imidodiphosphate), and the absence of nucleotides (nucleotide-free) on complex formation under reducing and oxidizing conditions (Fig. 1 and *SI Appendix*, Fig. S2). A single-site binding model was used to fit the data and determine the thermodynamic parameters (*SI Appendix*, Table S2). Notably, entropic and enthalpic contributions largely varied with the oxidation state and bound nucleotide but compensated each other to give low micromolar dissociation constants under all conditions, regardless of oxidation state or the presence or absence of nucleotides (Fig. 1).

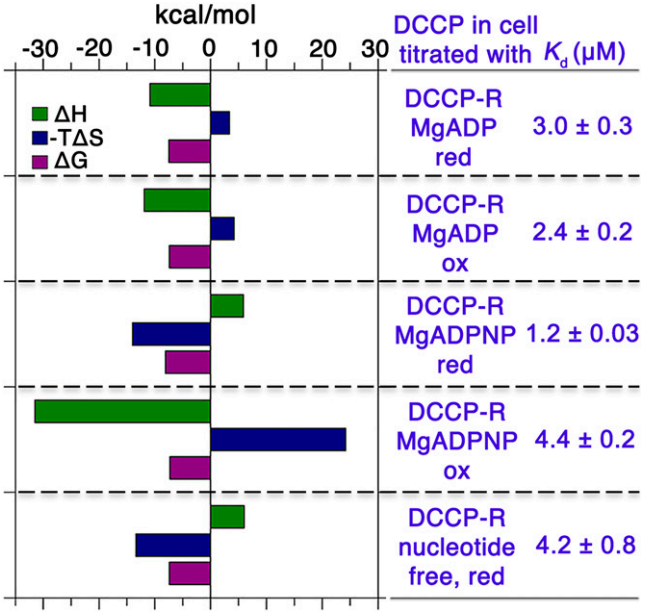

Fig. 1. Thermodynamic parameters for complex formation between DCCP and DCCP-R. Oxidizing (ox) and reducing (red) conditions are indicated. The numbers of binding sites were above 0.7 for all experiments. Detailed thermodynamic values for changes in entropy (ΔS), enthalpy (ΔH), and Gibbs free energy (ΔG) are in *SI Appendix*, Table S2.

In the reverse experiment, we investigated the affinity of DCCP-R alone and the DCCP-R:DCCP complex for the nucleotides MgADP and MgADPNP. The binding of both nucleotides was enthalpically driven with low K_d values (MgADP: $K_d = 42 \pm 7$ μM; MgADPNP: $K_d = 15 \pm 0.5$ μM) (*SI Appendix*, Fig. S2 *F–I* and Table S2). Although there are two nucleotide binding sites in the homodimeric DCCP-R, the titration data could be fitted by a model containing identical binding sites giving a single K_d, indicating the same binding affinity for both ATP binding sites. The additional presence of DCCP in the titration cell changed the enthalpic and entropic contributions but not the affinity (MgADPNP: $K_d = 7.1 \pm 1.1$ μM).

Redox potential changes upon complex formation and nucleotide-binding. Next, we investigated whether the redox potential changed upon complex formation and nucleotide-binding in order to trigger ET. For this, we isolated DCCP:DCCP-R in the presence of MgADP under oxidizing conditions (*SI Appendix*, Fig. S1*F*) and investigated its reaction with reducing agents using ultraviolet-visible (UV-vis) spectroscopy. While the [4Fe4S] cluster in DCCP-R alone was easily reducible by DT, the DC cluster in DCCP was resistant to reduction by DT or Ti(III)-citrate (13). The UV-vis absorption spectrum of the oxidized complex had a maximum of approximately 400 to 420 nm (red-trace 1 in *SI Appendix*, Fig. S3*A*). Adding DT immediately decreased absorbance at 420 nm, which was stable for 20 min and likely originated only from the reduction of the [4Fe4S] cluster (blue-trace 2 in *SI Appendix*, Fig. S3*A*). Further bleaching of the visible spectrum was only possible by adding MgATP, with reduction occurring with an observed rate constant (k_{obs}) of 0.68 min^{-1}, similar to previous findings (13). This finding showed that the redox potential of the [4Fe4S] cluster does not decrease significantly upon complex formation. Further, we investigated whether electron transfer from DCCP-R to DCCP is triggered by the binding of MgATP alone or whether its hydrolysis is required (*SI Appendix*, Fig. S3*B*). After adding MgATP, the absorbance at 420 nm decreased exponentially with a k_{obs} of 0.71 min^{-1}.

In contrast, adding MgADPNP (K_d of 7.1 μM in DCCP:DCCP-R_{red}) did not change absorbance. We also examined whether the ATPase activity of DCCP-R in the complex differed in the oxidized and reduced states (*SI Appendix*, Fig. S3*C*), which was not the case, as previously reported (13). We concluded that electron transfer from DCCP-R to DCCP is not triggered by the binding of MgATP but requires its hydrolysis.

Structural analyses of DCCP:DCCP-R complexes. To gain insights into the spatial interplay between the cofactors, we resolved the DCCP:DCCP-R complex in three different catalytically relevant states: 1) with MgADPNP at a resolution of 1.82 Å, 2) with MgADP-AlF_4 as a transition state analog of ATP hydrolysis at a resolution of 1.96 Å, and 3) nucleotide-free at a resolution of 3.25 Å (*SI Appendix*, Table S3). All states were cocrystallized, and crystals belonged to space group *P*1 with similar cell constants (*SI Appendix*, Table S3).

Overall complex structure. We describe the MgADPNP containing structure as follows. We resolved two almost identical DCCP:DCCP-R:MgADPNP complexes in the asymmetric unit with an rmsd of 0.73 Å for C_α-atoms and dimensions of 85 Å × 80 Å × 90 Å (Fig. 2*A*). The twofold symmetry axes of DCCP and DCCP-R were aligned so that the complex preserved the twofold symmetry. Accordingly, the [4Fe4S] cluster of DCCP-R lay on the symmetry axis so that its shortest distance to the nearest atoms of the two β-subclusters of DCCP was ∼17 Å (Fig. 2), slightly longer than typically found in ET chains (35).

Complex interface. We used the Proteins, Interfaces, Structures and Assemblies server (https://www.ebi.ac.uk/msd-srv/prot_int/pistart.html) to analyze the molecular interfaces (*SI Appendix*, Fig. S3*D*). Upon complex formation, approximately 11% of the accessible surface area (ASA) of the DCCP dimer and 15% ASA of the DCCP-R dimer were buried in the DCCP:DCCP-R interface (Fig. 2). The large DCCP:DCCP-R interface agreed well with the stability of the complex observed in solution (Fig. 1 and *SI Appendix*, Fig. S1). A predominantly electrostatic stabilization of the complex was indicated by the electrostatic surface potential (Fig. 3), with large areas of opposing charges in the interface—a broad ring of negative charge around a hydrophobic patch in DCCP and overall positive charges in DCCP-R, especially around the [4Fe4S] cluster. See *SI Appendix*, Fig. S4*C* and Table S4 for relevant interactions.

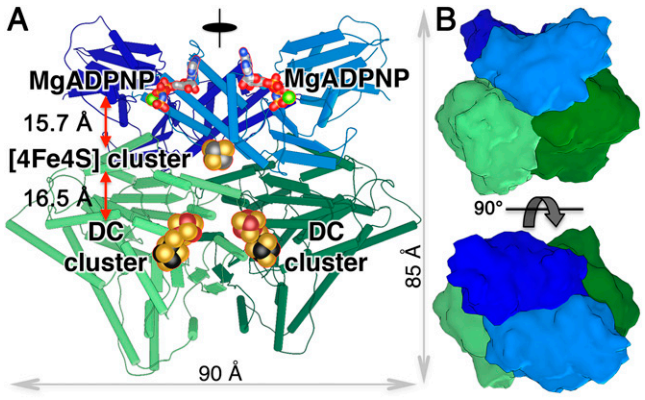

Fig. 2. Overall structure of DCCP:DCCP-R in complex with MgADPNP. (*A*) A side view of the complex as ribbon representation. Fe/S clusters are drawn as spheres with Fe in three colors (gray Fe for [4Fe4S] cluster, dark red Fe for β-subclusters, and black Fe for α-subclusters of the DC clusters. S is colored gold). (*B*) Surface representation of the complex. Colors as for the ribbon presentation in (*A*).

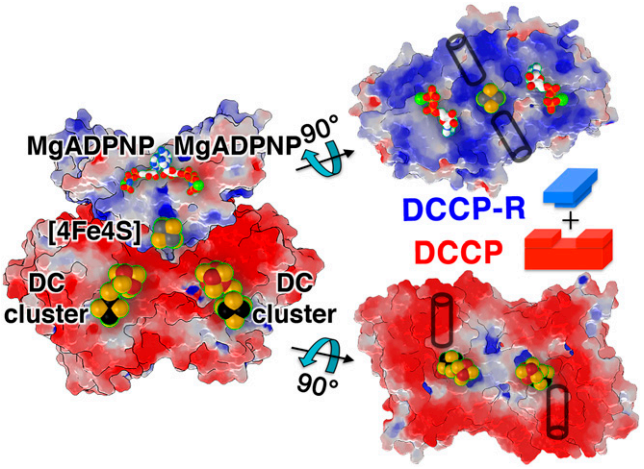

Fig. 3. Intermolecular interface of the DCCP:DCCP-R structure. Electrostatic surface representation calculated using the adaptive Poisson-Boltzman solver APBS (36). Electrostatic surface potentials are colored ranging from red at −5 kT/e to blue at +5 kT/e. The positions of the C-terminal helix of DCCP and H7 in DCCP-R are marked as cylinders.

DCCP structure. The structures of DCCP alone (13) and in complex with DCCP-R were overall identical, as reflected by an rmsd of 0.28 Å for C_α-atoms after superposition. However, two changes in the complex interface were noteworthy (*SI Appendix*, Fig. S4 *A* and *B*). First, the C-terminal α-helix interacting with DCCP-R in the complex showed higher than average B-factors in DCCP alone but below average B-factors in the complex (*SI Appendix*, Fig. S4*A*), indicating that it was stabilized upon complex formation. The main-chain atoms of the α-helix moved approximately 1 Å and some of the side chains adopted different rotamers involved in H-bonding interactions with residues from the cluster helix H7 (see below), loop L12 contacting H6 and H7 in DCCP-R and DCCP:Q408 interacts with DCCP-R:Q93 at the phosphate-binding site of DCCP-R (*SI Appendix*, Fig. S4*C* and Table S4). Second, the loop leading to the α-helix (C-terminal loop, D400 to D405) shifted by ∼3.5 Å (*SI Appendix*, Fig. S4*B*). No changes were visible near the DC cluster, and the entrances to the two substrate channels remained open in the complex.

DCCP-R structure. In contrast to DCCP, the structure of DCCP-R alone is unknown. DCCP-R is a homodimer covalently bridged by a [4Fe4S]-cluster positioned along the twofold rotation axis of the dimer (Figs. 2*A* and 4*A* and *SI Appendix*, Fig. S5*A*). The DCCP-R dimer is additionally stabilized by an extensive interface covering ∼13% of the ASA of each subunit (Fig. 4*B* and *SI Appendix*, Figs. S3*C* and S6*A*).

Each subunit houses MgADPNP at a nucleotide-binding site (Fig. 4 *A* and *B*) and can be divided into three domains: domains I and II and the Fe/S-domain (Fig. 4*A* and *SI Appendix*, Fig. S6*B*). Domains I and II have the characteristic $\beta\beta\beta\alpha\beta\alpha\beta\alpha$ topology of the ASKHA-fold superfamily (37) and contribute to binding MgADPNP (Fig. 4*A*). A search for structures of similar fold (38) and a sequence alignment (*SI Appendix*, Fig. S6*C*) supported the homology of DCCP-R to other members of the ASKHA superfamily, with the highest scores for the activators of HADs (*SI Appendix*, Table S5). The Fe/S-domain contains four α-helices (H4, H6–H8; Fig. 4*A* and *SI Appendix*, Fig. S6*B*), of which H4 and H7 harbor the two conserved cysteines (C115, C152) coordinating the [4Fe4S] cluster (Fig. 4 *A* and *C*). Notably, C152 is located at the N-terminal end of the α-helix pair H7/H7* (cluster helix). This HCH arrangement forms

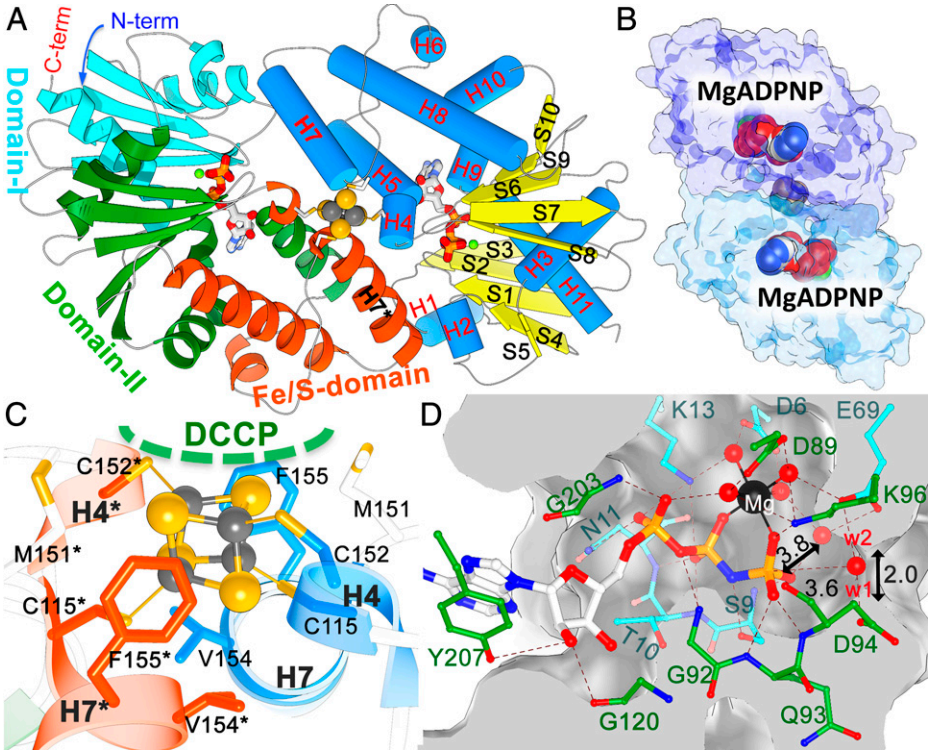

Fig. 4. Crystal structure of MgADPNP-bound DCCP-R in the complex. (*A*) Overall structure of the DCCP-R homodimer. In the left subunit, the three domains are colored differently. Mg^{2+} ions are shown as black spheres. (*B*) Surface representation along the entrance to the nucleotide-binding site. (*C*) [4Fe4S] cluster environment. Residues and helices are domain-colored as in (*A*). Residues marked with asterisks are from the symmetry-related subunit. (*D*) Binding pocket for MgADPNP. Dashed lines show direct interactions with side chains and solvent molecules. Residues are domain-colored as in (*A*). Water molecules are shown as red spheres.

an angle of 125°. The [4Fe4S] cluster core is not in H-bonding distance to potential donors and is shielded from the solvent by hydrophobic residues (Fig. 4*C*). One of the [2Fe2S]-rhombs of the [4Fe4S] cluster lies directly at the DCCP:DCCP-R interface, where it is shielded from the solvent by DCCP (Fig. 2*A*). Complex formation allows H-bond formation between S_δ-Cys115 coordinating the [4Fe4S] cluster and N111 in DCCP (*SI Appendix*, Fig. S4*C*).

Simulated annealing F_{obs}-F_{calc} omit electron density maps clearly define the binding mode of MgADPNP in both subunits (*SI Appendix*, Fig. S5*B*). The phosphates are positioned at the V-shaped junction of the β-sheets of domains I and II, and the adenosine moiety lies between helices H5 and H10 (Fig. 4*A*). The adenosine has few interactions with the protein (Fig. 4*D*). In contrast, the three phosphate groups are tightly bound by a network of H-bonds with residues S9 to N11 and Q92 to D94 (Fig. 4*D*). These residues are well conserved among homologs of DCCP-R (*SI Appendix*, Fig. S6*C*). The β- and γ-phosphates bind an Mg^{2+} ion whose octahedral coordination is completed by four water molecules (*SI Appendix*, Fig. S5*D*).

ATP hydrolysis by DCCP-R. We observed two water molecules, w1 and w2, near the γ-phosphate (Fig. 4*D*). Water 1 would be a suitable candidate for the nucleophile (lytic water) in an inline attack, and w2 could act as a base in connection with D94 or E69 (*SI Appendix*, Fig. S7*A*). A small opening with ~2 Å diameter next to w1 could provide the water supply for the reaction (Fig. 4*D* and *SI Appendix*, Fig. S7*B*). To access the role of E69 as a base, we compared the rates of ATP hydrolysis between wild type and two variants, E69Q and E69N (*SI Appendix*, Fig. S7*C*). The activity of the wild type was 8.0 ± 0.2 nmol/min/mg at 22 °C, comparable to previously reported activity (13), but the rates were approximately 10-fold lower for the two variants (0.5 ± 0.1 nmol/min/mg for E69Q and 0.9 ± 0.4 nmol/min/mg for E69N), supporting the potential role of E69 as a redundant catalytic base.

Network of H-bonds in the complex. The DCCP:DCCP-R complex has two H-bonding networks stretching from the phosphate-binding site via the [4Fe4S] cluster in DCCP-R close to the DC cluster in DCCP (Fig. 5), which could enable the propagation of conformational changes between the three cofactors. The first network starts at the highly conserved residues G92 and Q93 in the phosphate-binding site of DCCP-R and continues through H-bonds mediated by water from S158* in H7* to K114 in H4. These H-bond interactions are present in both subunits of DCCP-R. In the second network,

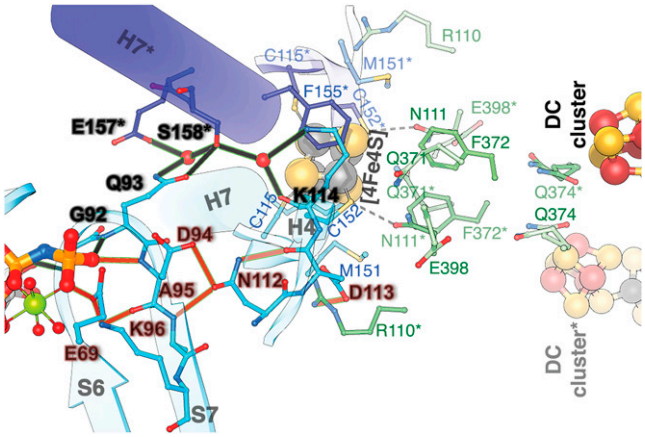

Fig. 5. Hydrogen-bonding networks. The two observed H-bonding networks from the phosphate-binding site to the [4Fe4S] cluster of DCCP-R are shown as black and orange lines. Residues marked with asterisks are from the symmetry-related subunit.

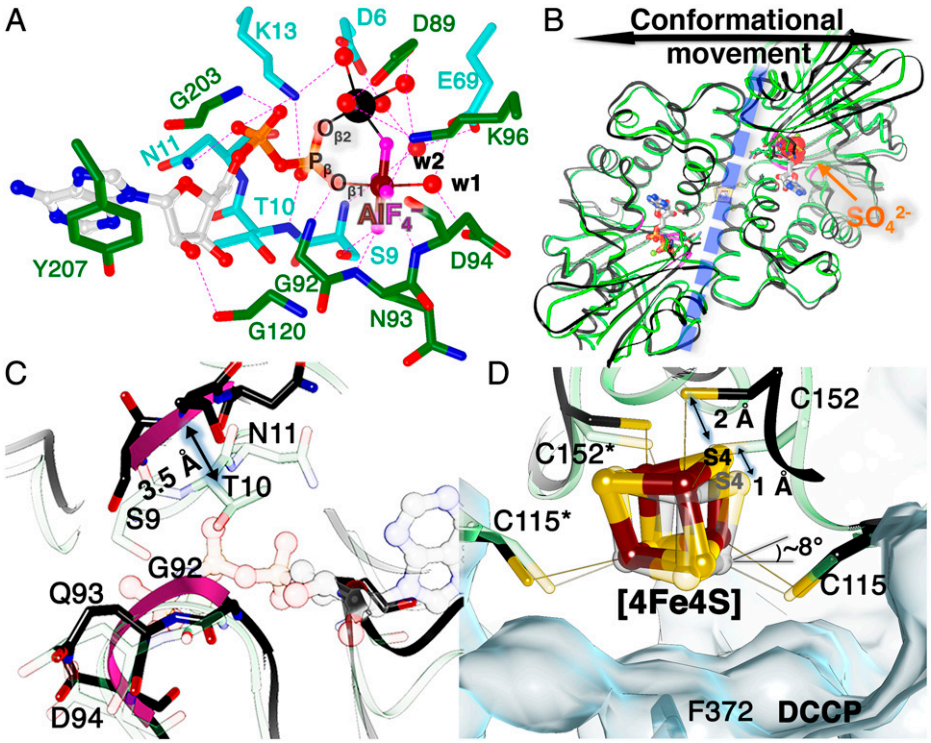

Fig. 6. Structures of DCCP:DCCP-R with bound MgADP-AlF_4^- and without nucleotide. (*A*) Interaction of MgADP-AlF_4^- in DCCP-R. Colors as in Fig. 4*D*. Dashed lines show potential H-bonds. (*B*) Superposition of nucleotide-free DCCP-R (black ribbon) with MgADPNP-bound DCCP-R (light green ribbon). A blue dashed line shows the center of the dimer. Comparisons of the phosphate-binding site (violet) (*C*) and the [4Fe4S] cluster (*D*) between the MgADPNP-bound and the nucleotide-free DCCP-R structures. The structure of MgADPNP-bound DCCP-R is shown with high transparency. Surface of DCCP from the nucleotide-free structure is shown in light blue. Black arrows show changes in structures.

the interactions start at E69 and proceed through K96 and D94 in the phosphate-binding site to residues N112 and D113 in the N terminus of the loop associated with H4. The two networks converge at the [4Fe4S] cluster and helices H4 and H7.

Structures of DCCP:DCCP-R with MgADP-AlF_4^--bound. Next, we analyzed the complex in two other catalytically relevant states: with bound MgADP-AlF_4^-, which approximates the transition state, and without a nucleotide. The overall structure of DCCP:DCCP-R:MgADP-AlF_4^- is indistinguishable from that of the MgADPNP-bound complex, as reflected by an rmsd of 0.24 Å for C_α atoms. The electron density clearly defines the octahedrally coordinated AlF_4^- next to an MgADP moiety (*SI Appendix*, Fig. S5*C*), whose coordination is completed by $O_{\beta1}$ and a water molecule (w1 in Fig. 6*A*) as axial ligands. Residues in contact with the γ-phosphate of MgADPNP are now oriented to accommodate AlF_4^- (Fig. 6*A* and *SI Appendix*, Fig. S5*E*). The Al ion is inline with $O_{\beta1}$ and w1 with an $O_{\beta1}$-Al-O_{W1} angle of 175° and a distance of 4.2 Å between the two oxygen atoms (*SI Appendix*, Fig. S5*E*). This mimics an anionic transition state for phosphoryl transfer during ATP hydrolysis with $O_{\beta1}$ as the leaving group and w1 as the lytic nucleophile (2).

Structure of nucleotide-free DCCP:DCCP-R. Despite the lower resolution of the nucleotide-free complex structure, the main chain and side chains are clearly defined for most parts of the protein in the $2F_{obs}$-F_{calc} electron density map (*SI Appendix*, Fig. S8*B*). A sulfate ion occupies the same position as the β-phosphate of ADPNP in one of the two DCCP-R subunits. When using the DCCP dimer as a reference, we found that conformational changes compared to the nucleotide-bound states of the complex, especially in DCCP-R are obvious (Fig. 6*B*). While the DCCP dimer structures superimpose with an rmsd of 0.53 Å at C_α-atoms, the DCCP-R structures deviate by ∼2.0 Å rmsd for the C_α atoms, originating from a motion of one subunit away from the [4Fe4S] cluster (Fig. 6*B*). This movement increases the HCH angle by ∼2° and elongates the conformation of DCCP-R. In addition, the phosphate-binding site opens with a movement of 3.5 Å for the C_α-atom of T10 (Fig. 6*C*), and the channel for the transport of substrate waters widens (*SI Appendix*, Fig. S7*B*). The changes also extend to the [4Fe4S] cluster with a ∼2 Å shift of the S_γ atom of C152, accompanied by a move of the [4Fe4S] cluster away from the surface of DCCP (Fig. 6*D*). Compared to the structure with bound MgADPNP, the [4Fe4S] cluster of nucleotide-free DCCP:DCCP-R is tilted ∼8° away from the surface of DCCP. The sulfate ion in only one subunit of DCCP-R likely contributes to the observed asymmetry (Fig. 6*B*). The conformational rearrangements also disrupt the intermolecular salt bridge involving D113 in H4 of DCCP-R and R110 of DCCP (*SI Appendix*, Fig. S4*C*). While the conformational changes are small in the center of the nucleotide-free DCCP-R dimer, they amplify outward to form an elongated structure (Fig. 6*B*). The conformational changes associated with nucleotide release also disrupt the H-bond networks between nucleotide-binding site, [4Fe4S], and the DC clusters found in the nucleotide-bound states at the H-bond pairs Q93:S158, D94:N112 and A95:N112 (*SI Appendix*, Fig. S9).

Discussion

Complex formation. Controlled complex formation is used in the electron-transferring ATPases to ensure the unidirectional electron flow, typically in response to the nucleotide-binding and/or redox state of the cofactors (2, 4, 8, 18, 19, 31, 33, 39). Whereas transient protein complexes tend to form small and poorly packed interfaces for ET (40, 41), the interface of the

DCCP:DCCP-R complex is densely packed with many H-bonding interactions and pronounced surface complementarity (Fig. 4 and *SI Appendix*, Fig. S4*C*). Correspondingly, we observed moderately stable complexes for DCCP:DCCP-R under all conditions tested.

Is DCCP-R an archerase? For the activators, also known as archerases, a conformational switch resembling the shooting of a bow has been proposed, with the HCH unit as the bowstring (11, 12). Given the structural similarity of both ATPases and both catalytic units and the conservation of residues stabilizing the DCCP:DCCP-R complex (*SI Appendix*, Fig. S6*C*), similar overall complexes are likely. However, when we superimposed the activators with DCCP-R in the complex, large steric clashes with their catalytic unit resulted (*SI Appendix*, Fig. S8*D*). These could only be avoided when the HCH angle of 95° to 105°, found in the activators (33, 34), would widen to the 125° to 127° observed in the DCCP:DCCP-R complex, including an inward rotation of ∼60° (*SI Appendix*, Fig. S8*C*). The widening would bring the [4Fe4S] cluster closer to the complex interface. Thus, the structure of DCCP:DCCP-R supports the central prediction of the conformational switch in archerases that the HCH bowstring has to move to fire its arrows.

However, is the archerase switch also underlying the ATPase-coupled electron transfer in DCCP:DCCP-R? We cannot exclude it, but the very different coupling between ATPase activity and complex formation in the two systems speaks against it. In the archerases, ATP binding controls complex formation and, conversely, complex formation stimulates ATPase activity (42). In contrast, in DCCP-R, protein complex formation and ATP binding are independent and complex formation stimulates the ATPase activity only weakly (13). This seems to argue against a role for large and affinity-controlling conformational changes in DCCP-R. However, if DCCP-R does not act like an archerase, how may ATPase activity and ET be coupled?

How the triad MgATP-[4Fe4S]-DC is connected. One alternative to the large conformational changes of the archerase switch is local conformational changes emanating from the nucleotide-binding site and continuing to the Fe/S-clusters. The two H-bonding networks extending from the phosphate-binding site to the DC cluster (Fig. 5) may allow this propagation of conformational changes. The nucleotide-dependent structural changes we observed in the DCCP:DCCP-R complex allow a first impression of how nucleotide-induced conformational changes may be linked to the ET process (Fig. 7*A*). Starting the cycle, we postulated a complex with an extended HCH conformation of DCCP-R, as seen in the nucleotide-free DCCP:DCCP-R structure (state 1 in Fig. 7*A*). The [4Fe4S] cluster of DCCP-R may be oxidized or reduced at the start, as it remains reducible in the protein complex. The binding of MgATP induces a more compact state of DCCP-R and forms the extended H-bonding networks (state 2 in Fig. 7*A*). However, as the DCCP:DCCP-R:MgADP-AlF_4^- complex shows, the hydrolysis of ATP to ADP + Pi is likely not sufficient to induce the required conformational change to trigger ET (state 3 in Fig. 7*A*). The largest conformational changes occur when ADP and Pi are released, disrupting the H-bonding networks and simultaneously changing the positions of the coordinating cysteines of the [4Fe4S] cluster. This may trigger ET toward the DC cluster along a pathway that includes the hydrophobic region of DCCP (Fig. 5). DCCP then uses the electrons to reduce a substrate (state 4 in Fig. 7*A*). To conclude the cycle, DCCP-R returns to the extended HCH state (state 1), in which it is again receptive to electron(s) and MgATP.

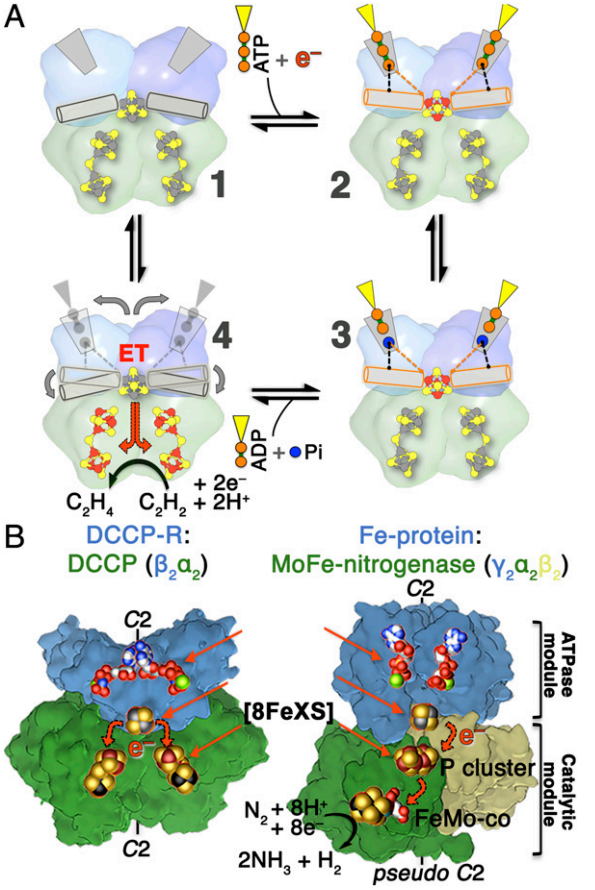

Fig. 7. Mechanism of ATP-coupled electron transfer (*A*) and comparison of the DCCP and nitrogenase complexes (*B*). (*A*) ET driven by conformational changes upon ATP hydrolysis. States 1–3 are modeled after the structures: 1) after nucleotide-free DCCP:DCCP-R, 2) after DCCP:DCCP-R:MgADPNP, and 3) after DCCP:DCCP-R:MgADP-AlF_4^-. The surfaces of DCCP and DCCP-R are colored as in Fig. 2. The black and orange dotted lines represent the H-bond networks shown in panel A-2 and -3. Iron atoms with gray spheres show a more oxidized state than iron atoms with red color. Gray arrows in state 4 show conformational switch, as observed in the nucleotide-free DCCP:DCCP-R structure, triggering ET after ATP hydrolysis. The gray area of DCCP-R shows the open ATP binding site. The HCH helices are shown as cylinders. (*B*) Comparison of the DCCP:DCCP-R and Fe-protein:MoFe-nitrogenase complexes.

This rough mechanistic sketch is certainly incomplete. Our SEC and ITC data already show that in the ADPNP-bound oxidized state a more compact DCCP:DCCP-R structure forms than in the reduced state, supported by the smaller apparent mass in the SEC (*SI Appendix*, Table S1) and a substantially higher binding enthalpy ($\Delta H_{ox} = -31.5$ kcal/mol vs. $\Delta H_{red} =$ 5.9 kcal/mol; *SI Appendix*, Table S2). This shows that the oxidation state of the [4Fe4S] cluster changes the structure of the DCCP:DCCP-R complex. It is tempting to assume that the observed long distance between [4Fe4S] and the DC cluster in our oxidized structures shrinks in the reduced state to allow facile electron transfer while slowing down the unproductive reverse electron transfer from the reduced DC to the oxidized [4Fe4S] cluster by increasing the distance.

ATPase-coupled ET in DCCP and nitrogenase. Despite belonging to different NTPase-families with different core folds and therefore independent evolution, the complexes of the Fe protein and DCCP-R feature very similar architectures (Fig. 7*B*), starting with the overall twofold symmetry of the complexes. Here, the DCCP:DCCP-R complex is twofold-symmetric

throughout, while in the nitrogenase complex the twofold symmetry axis of the Fe protein aligns with a pseudo-twofold symmetry of the MoFe protein (2, 14–16). In both cases, two ATPase sites act on a single [4Fe4S] cluster—in sum, allowing the transmission of a ∼100 kJ/mol power stroke. Furthermore, the two protein complexes create similar arrangements for their cofactors. In both ATPases, the bound nucleotides point their phosphates toward the [4Fe4S] clusters with distances between gamma-phosphate and the [4Fe4S] cluster of 15 Å to 16 Å, and the shortest Fe–Fe distances between [4Fe4S] clusters and the electron-accepting [8FeXS] cluster (X = 9 for the DC cluster; X = 7 for the P-cluster) of 16–17 Å. Thus, both complexes position very similar cofactors almost identically to couple ET and ATP hydrolysis.

How the three cofactors communicate is not fully understood. In both cases, one would expect yet-unknown conformational changes during ATP hydrolysis to enable the ET. In the MoFe nitrogenase (2, 4, 18, 19, 21, 39) the Fe protein allows communication via its switch I and II regions (2, 43, 44). By modulating the redox potential of the [4Fe4S] cluster and being part of a H-bonding network extending from the P-loop to the [4Fe4S] cluster (2, 43, 44), switch II is clearly analogous to the HCH domain and its H-bond network in DCCP:DCCP-R (Fig. 5).

The similarities between the nonhomologous nitrogenase and DCCP systems are an example for a convergent evolution toward similar catalytic strategies to couple ATPase activity with electron transfer between Fe/S centers.

Materials and Methods

Further details of the materials and methods are available in the *SI Appendix*.

Protein production. We produced DCCP and DCCP-R variants as described previously (13).

UV-vis spectrophotometry. UV-vis spectra were recorded at 25 °C using a diode-array spectrophotometer housed inside a COY glove box (COY). For the ATP hydrolysis–dependent ET assay, a ∼1:2 molar ratio of DCCP to DCCP-R in 50 mM Tris·HCl pH 8.0 was mixed with an excess of DT. We monitored time-dependent absorbance changes at 420 nm after adding ATP or ATP analogs.

SEC. We investigated complex formations of DCCP and DCCP-R in solution under different conditions using a Superdex S-200 prep-grade column (10 × 300 mm) equilibrated in 50 mM Tris·HCl pH 8.0. DCCP was mixed with DCCP-R in a molar ratio of 1:2 and loaded on the column after 10 min incubation.

ITC. We performed ITC experiments using a MicroCal VP-ITC at 25 °C, housed in an anoxic glovebox (Labstar workstation, MBRAUN, Germany) with an atmosphere of N_2 containing less than 0.5 ppm O_2. An ITC buffer of 50 mM Tris·HCl pH 8.0 was used to dissolve all proteins and ligands. We freshly buffered protein samples with the ITC buffer using a G25 column before the titration experiment.

Complex formation and crystallization. The complex DCCP:DCCP-R with MgADPNP or MgADP-AlF_4^- was formed by mixing appropriate components in 20 mM Tris·HCl pH 8.0. After 60 min incubation, we removed excess DCCP-R by a spin concentrator and concentrated the solution to ∼30 mg/mL protein complex, which was directly used for crystallization. We crystallized proteins by the sitting-drop vapor diffusion method by mixing equal volumes of protein with a reservoir solution at 18 °C. All crystals of DCCP:DCCP-R complexes containing MgADPNP and MgADPAlF_4^- were obtained in a solution of 0.15 M to 0.225 M ammonium sulfate, 0.1 M Tris·HCl pH 8.0, and 13 to 15% (wt/vol) polyethylene glycol (PEG) 4000. The nucleotide-free DCCP:DCCP-R complex was crystallized in a condition containing 0.2 M ammonium sulfate, 0.1 M Tris·HCl pH 8.0, and 10% (wt/vol) PEG 8000.

Data collection and structure refinements. We collected diffraction data at 100 K on a beamline BL 14.1 operated using the Helmholtz-Zentrum at the BESSY II electron storage ring (Berlin, Germany) (45). The structure of the DCCP:DCCP-R complex was solved by Patterson search techniques using 6ENO.pdb (13) as an initial search model for DCCP. DCCP-R was built initially from electron density after the phasing and was refined using standard crystallographic methods.

Data Availability. Coordinate and structure factor amplitude are available at the Protein Data Bank (PDB), www.wwpdb.org, under accession numbers 7YZM for DCCP:DCCP-R:MgADPNP (46), 7YZQ for DCCP:DCCP-R:MgADP-$AlF4^-$(47), and 7YYL for DCCP:DCCP-R (48) without nucleotides. All study data are included in the article and/or *SI Appendix*.

ACKNOWLEDGMENTS. We acknowledge access to beamlines of the BESSY II storage ring (Berlin) through the Joint Berlin MX-Laboratory sponsored by Helmholtz Zentrum Berlin für Materialien und Energie, Freie Universität Berlin, Humboldt-Universität zu Berlin, Max-Delbrück-Centrum, and the Leibniz-Institut für Molekulare Pharmakologie. This work is funded by the Deutsche Forschungsgemeinschaft (DFG, German Research Foundation) under Germany's Excellence Strategy – EXC 2008 – 390540038 – UniSysCat and DFG project DO 785/8-1.

1. J.-H. Jeoung, B. M. Martins, H. Dobbek, Double-cubane [8Fe9S] clusters: A novel nitrogenase-related cofactor in biology. *ChemBioChem* **21**, 1710–1716 (2020).
2. H. Schindelin, C. Kisker, J. L. Schlessman, J. B. Howard, D. C. Rees, Structure of ADP x AlF4(-)-stabilized nitrogenase complex and its implications for signal transduction. *Nature* **387**, 370–376 (1997).
3. Y. Hu, M. W. Ribbe, Nitrogenase and homologs. *J. Biol. Inorg. Chem.* **20**, 435–445 (2015).
4. H. L. Rutledge, F. A. Tezcan, Electron transfer in nitrogenase. *Chem. Rev.* **120**, 5158–5193 (2020).
5. A. Siebert, T. Schubert, T. Engelmann, S. Studenik, G. Diekert, Veratrol-O-demethylase of *Acetobacterium dehalogenans*: ATP-dependent reduction of the corrinoid protein. *Arch. Microbiol.* **183**, 378–384 (2005).
6. T. Ferguson, J. A. Soares, T. Lienard, G. Gottschalk, J. A. Krzycki, RamA, a protein required for reductive activation of corrinoid-dependent methylamine methyltransferase reactions in methanogenic archaea. *J. Biol. Chem.* **284**, 2285–2295 (2009).
7. A. Schilhabel *et al.*, The ether-cleaving methyltransferase system of the strict anaerobe *Acetobacterium dehalogenans*: Analysis and expression of the encoding genes. *J. Bacteriol.* **191**, 588–599 (2009).
8. S. E. Hennig, J.-H. Jeoung, S. Goetzl, H. Dobbek, Redox-dependent complex formation by an ATP-dependent activator of the corrinoid/iron-sulfur protein. *Proc. Natl. Acad. Sci. U.S.A.* **109**, 5235–5240 (2012).
9. M. Boll, Key enzymes in the anaerobic aromatic metabolism catalysing Birch-like reductions. *Biochim. Biophys. Acta* **1707**, 34–50 (2005).
10. W. Buckel, J. W. Kung, M. Boll, The benzoyl-coenzyme a reductase and 2-hydroxyacyl-coenzyme a dehydratase radical enzyme family. *ChemBioChem* **15**, 2188–2194 (2014).
11. J. Kim, M. Hetzel, C. D. Boiangiu, W. Buckel, Dehydration of (R)-2-hydroxyacyl-CoA to enoyl-CoA in the fermentation of α-amino acids by anaerobic bacteria. *FEMS Microbiol. Rev.* **28**, 455–468 (2004).
12. W. Buckel *et al.*, Enzyme catalyzed radical dehydrations of hydroxy acids. *Biochim. Biophys. Acta* **1824**, 1278–1290 (2012).
13. J.-H. Jeoung, H. Dobbek, ATP-dependent substrate reduction at an [Fe_8S_9] double-cubane cluster. *Proc. Natl. Acad. Sci. U.S.A.* **115**, 2994–2999 (2018).
14. D. C. Rees *et al.*, Structural basis of biological nitrogen fixation. *Philos. Trans.- Royal Soc., Math. Phys. Eng. Sci.* **363**, 971–984 (2005).
15. J. B. Howard, D. C. Rees, Structural basis of biological nitrogen fixation. *Chem. Rev.* **96**, 2965–2982 (1996).
16. O. Einsle, D. C. Rees, Structural enzymology of nitrogenase enzymes. *Chem. Rev.* **120**, 4969–5004 (2020).
17. M. M. Georgiadis *et al.*, Crystallographic structure of the nitrogenase iron protein from *Azotobacter vinelandii*. *Science* **257**, 1653–1659 (1992).
18. L. Chen *et al.*, MgATP-induced conformational changes in the iron protein from *Azotobacter vinelandii*, as studied by small-angle X-ray scattering. *J. Biol. Chem.* **269**, 3290–3294 (1994).
19. B. K. Burgess, D. J. Lowe, Mechanism of molybdenum nitrogenase. *Chem. Rev.* **96**, 2983–3012 (1996).
20. D. J. Lowe, R. N. Thorneley, The mechanism of *Klebsiella pneumoniae* nitrogenase action. The determination of rate constants required for the simulation of the kinetics of N_2 reduction and H_2 evolution. *Biochem. J.* **224**, 895–901 (1984).
21. L. C. Seefeldt *et al.*, Energy transduction in nitrogenase. *Acc. Chem. Res.* **51**, 2179–2186 (2018).
22. M. Rohde, C. Trncik, D. Sippel, S. Gerhardt, O. Einsle, Crystal structure of VnfH, the iron protein component of vanadium nitrogenase. *J. Biol. Inorg. Chem.* **23**, 1049–1056 (2018).
23. D. Sippel, O. Einsle, The structure of vanadium nitrogenase reveals an unusual bridging ligand. *Nat. Chem. Biol.* **13**, 956–960 (2017).
24. M. Rohde, K. Grunau, O. Einsle, CO binding to the FeV cofactor of CO-reducing vanadium nitrogenase at atomic resolution. *Angew. Chem. Int. Ed. Engl.* **59**, 23626–23630 (2020).
25. J. Moser *et al.*, Structure of ADP-aluminium fluoride-stabilized protochlorophyllide oxidoreductase complex. *Proc. Natl. Acad. Sci. U.S.A.* **110**, 2094–2098 (2013).
26. S. E. Hennig *et al.*, ATP-induced electron transfer by redox-selective partner recognition. *Nat. Commun.* **5**, 4626 (2014).

27. M. Sperfeld, G. Diekert, S. Studenik, Kinetic regulation of a corrinoid-reducing metallo-ATPase by its substrates. *Mol. Microbiol.* **92**, 598–608 (2014).
28. H. Dürichen, G. Diekert, S. Studenik, Redox potential changes during ATP-dependent corrinoid reduction determined by redox titrations with europium(II)-DTPA. *Protein Sci.* **28**, 1902–1908 (2019).
29. F. Neumann, H. Dobbek, ATP binding and a second reduction enables a conformationally gated uphill electron transfer. *ACS Catal.* **11**, 8565–8575 (2021).
30. J. W. Kung *et al.*, Reversible biological Birch reduction at an extremely low redox potential. *J. Am. Chem. Soc.* **132**, 9850–9856 (2010).
31. J. Kim, A. J. Pierik, W. Buckel, A complex of 2-hydroxyisocaproyl-coenzyme A dehydratase and its activator from *Clostridium difficile* stabilized by aluminum tetrafluoride-adenosine diphosphate. *ChemPhysChem* **11**, 1307–1312 (2010).
32. S. H. Knauer, W. Buckel, H. Dobbek, Structural basis for reductive radical formation and electron recycling in (R)-2-hydroxyisocaproyl-CoA dehydratase. *J. Am. Chem. Soc.* **133**, 4342–4347 (2011).
33. S. H. Knauer, W. Buckel, H. Dobbek, On the ATP-dependent activation of the radical enzyme (R)-2-hydroxyisocaproyl-CoA dehydratase. *Biochemistry* **51**, 6609–6622 (2012).
34. K. P. Locher *et al.*, Crystal structure of the *Acidaminococcus fermentans* 2-hydroxyglutaryl-CoA dehydratase component A. *J. Mol. Biol.* **307**, 297–308 (2001).
35. C. C. Page, C. C. Moser, X. Chen, P. L. Dutton, Natural engineering principles of electron tunnelling in biological oxidation-reduction. *Nature* **402**, 47–52 (1999).
36. N. A. Baker, D. Sept, S. Joseph, M. J. Holst, J. A. McCammon, Electrostatics of nanosystems: Application to microtubules and the ribosome. *Proc. Natl. Acad. Sci. U.S.A.* **98**, 10037–10041 (2001).
37. J. H. Hurley, The sugar kinase/heat shock protein 70/actin superfamily: Implications of conserved structure for mechanism. *Annu. Rev. Biophys. Biomol. Struct.* **25**, 137–162 (1996).
38. L. Holm, L. M. Laakso, Dali server update. *Nucleic Acids Res.* **44**, W351-5 (2016).
39. L. C. Seefeldt *et al.*, Control of electron transfer in nitrogenase. *Curr. Opin. Chem. Biol.* **47**, 54–59 (2018).
40. J. Janin, Specific *versus* non-specific contacts in protein crystals. *Nat. Struct. Biol.* **4**, 973–974 (1997).
41. P. B. Crowley, M. A. Carrondo, The architecture of the binding site in redox protein complexes: Implications for fast dissociation. *Proteins* **55**, 603–612 (2004).
42. J. Kim, Y. Lu, W. Buckel, ATP- and redox-induced conformational changes in the activator of the radical enzyme 2-hydroxyisocaproyl-CoA dehydratase. *C. R. Chim.* **10**, 742–747 (2007).
43. D. Wolle, D. R. Dean, J. B. Howard, Nucleotide-iron-sulfur cluster signal transduction in the nitrogenase iron-protein: The role of Asp^{125}. *Science* **258**, 992–995 (1992).
44. S. B. Jang, L. C. Seefeldt, J. W. Peters, Insights into nucleotide signal transduction in nitrogenase: Structure of an iron protein with MgADP bound. *Biochemistry* **39**, 14745–14752 (2000).
45. U. Mueller *et al.*, The macromolecular crystallography beamlines at BESSY II of the Helmholtz-Zentrum Berlin: Current status and perspectives. *Eur. Phys. J. Plus* **130**, 141 (2015).
46. J-H. Jeoung, S. Nicklisch, H. Dobbek, Structural basis for coupled ATP-driven electron transfer in the double-cubane cluster protein. Protein Data Bank: 7YZM. https://www.rcsb.org/structure/unreleased/7YZM. Deposited 21 February 2022.
47. J-H. Jeoung, S. Nicklisch, H. Dobbek, Structural basis for coupled ATP-driven electron transfer in the double-cubane cluster protein. Protein Data Bank: 7YZQ. https://www.rcsb.org/structure/unreleased/7YZQ. Deposited 21 February 2022.
48. J-H. Jeoung, S. Nicklisch, H. Dobbek, Structural basis for coupled ATP-driven electron transfer in the double-cubane cluster protein. Protein Data Bank: 7YYL. https://www.rcsb.org/structure/unreleased/7YYL. Deposited 18 February 2022.